Redox-Induced Nucleation and Growth of Goethite on Synthetic Hematite Nanoparticles

Jeanette L. Voelz [a], William A. Arnold [b], R. Lee Penn [a,*] **(Revision 1)**

[a]*Department of Chemistry, University of Minnesota, Minneapolis, Minnesota, 55455*

[b]*Department of Civil, Environmental, and Geo- Engineering, University of Minnesota, Minneapolis, Minnesota, 55455*

*Corresponding author. Present address: 139 Smith Hall, 207 Pleasant Street SE, Minneapolis, MN 55455, USA. Fax: +1 (612) 626 7541. *E-mail address:* rleepenn@umn.edu (R. L. Penn).

Abstract

The iron (oxyhydr)oxides hematite (α-Fe_2O_3) and goethite (α-FeOOH) are natural and reactive minerals common in soils and sediments, and their adsorption of Fe(II) produces reactive surface sites that facilitate reduction of oxidized environmental pollutants. Single-exposure experiments with 4-chloronitrobenzene showed that hematite is more reactive than goethite, when normalized by surface area loading. Interestingly, the product of Fe(II) oxidation is a mixture of goethite and hematite, and the goethite to hematite ratio depends on the distribution of Fe(II) activated surface sites, which is a function of aqueous Fe(II) concentration, surface area loading, and pH. More goethite is produced under conditions of higher Fe(II), lower surface area loading, and higher pH. Recurrent-exposure experiments showed a substantial decrease in reaction rate after one to three exposures, a trend suggestive of reaction contributions from the increasing goethite surface area over time. Using known atomic surface geometry for goethite and hematite, the hematite {012} facet is proposed as the site of primary mineral growth with goethite {021} at the interface between the two minerals. These results have implications in contaminant fate

modeling, where the mineral phases present in the environment, the minerals likely to form, and the surrounding aqueous conditions all have an impact on contaminant reaction rate.

Introduction

Iron is one of the most abundant elements on Earth, and its oxides, oxyhydroxides, and hydroxides (collectively termed 'iron oxides') are currently tabulated at seventeen recognized crystal structures (Faivre 2016). Iron oxide minerals form in a range of mild to extreme environmental conditions, with phases produced dependent on temperature, pressure, pH, aqueous ion concentrations, hydration state, and oxygen fugacity (Schwertmann and Murad 1983; Cornell and Schwertmann 1996; Lagroix et al. 2016).

Anthropogenic influences, however, rapidly alter minerals, and the geological impacts of industrial activities like mining (Chopard et al. 2017; Valencia-Avellan et al. 2017) and agriculture (Maqueda et al. 2017) are still under investigation. The release of highly oxidized chemicals into reduced groundwaters facilitates redox reactions that not only transform the contaminants (Elsner et al., 2004a; Howard and Muir, 2013) but alter mineral surfaces as well (Chun et al. 2006; Strehlau et al. 2016). Minerals are recognized as important tools for environmental remediation via natural attenuation (Pecher et al., 2002; Elsner, et al., 2004b), permeable reactive barriers (Scherer et al. 2000), or *in-situ* redox manipulation (Boparai et al. 2008), but alterations from inadvertent anthropogenic influences must also be considered so that they are recognized, rather than mistaken for natural processes.

The specific adsorption of Fe(II) to iron oxide surfaces is known to occur through bidentate complexes with contiguous singly-coordinated hydroxyl group pairs (Wehrli et al. 1989; Barron

and Torrent 1996). The subsequent electron transfer to the bulk oxide results in the formation of new Fe(III) surface structures (Tanwar et al. 2008; Catalano et al. 2010) and activates these minerals for participation in redox reactions. This electron transfer process has been demonstrated for goethite and hematite using Mössbauer spectroscopy (Williams and Scherer 2004; Larese-Casanova and Scherer 2007; Rosso et al. 2010) and calculated in detail for hematite using molecular orbital calculations (Rosso et al. 2003). Many highly oxidized environmental contaminants, such as nitroaromatic compounds, are readily reduced when they encounter these Fe(II)-activated surfaces (Hofstetter et al. 1999; Dunnivant et al. 1992; Klausen et al. 1995; Ju and Parales 2010). Measuring the concurrent oxidative mineral growth provides important information about which surfaces were readily accessible to and most reactive with aqueous Fe(II) (Chun et al. 2006; Vindedahl et al. 2015; Strehlau et al. 2016).

It has been proposed that Fe(II) adsorption on hematite leads to magnetite precipitation (Jeon et al. 2001, 2003), but this proposal has not been supported in other works (Pedersen et al. 2005; Tanwar et al. 2008). Rather, observations of Fe(II) adsorption on hematite {012} by crystal truncation rod diffraction indicate that the oxidized surficial Fe(III) have Fe-O bond lengths of 1.93 – 2.18 Å, which is in agreement with Fe-O bond lengths in the bulk lattice of both goethite and hematite but not magnetite (Yang et al. 2006; Tanwar et al. 2008). These reports of Fe(III) surface structures resulting from the adsorption of Fe(II) on hematite are limited by the adsorption capacity of the mineral surface (Tanwar et al. 2008).

To further investigate the evolving mineralogy requires the addition of another electron-accepting species to oxidize Fe(II) beyond the adsorption capacity of the underlying hematite. For example, the model contaminant 4-chloronitrobenzene (4-ClNB) efficiently participates in redox reactions in systems containing iron oxides and Fe(II) (Elsner et al. 2004b; Vindedahl et

al. 2015; Strehlau et al. 2017). Oxidation of Fe(II) in suspensions of hematite may result in (1) hematite growth on existing hematite faces, (2) homogeneous nucleation of new particles, or (3) heterogeneous nucleation of new phases on existing hematite surfaces. Oxidative growth on goethite and hematite surfaces after the addition of Fe(II) and reaction with nitrobenzenes has been characterized using Mössbauer spectroscopy (Larese-Casanova et al. 2012). On hematite, the deposition of 4-6 monolayers of hematite was observed, followed by the formation of a new phase identifiable as goethite, which comprised 25 % and 95 % of the growth on hematite needles and hexagonal platelets, respectively. Changes to solution conditions (pH, buffer identity, ionic strength, and Fe(II) concentration) were not shown to have a profound effect on the monolayer onset of goethite formation on hematite, suggesting that goethite formation is instead a function of thermodynamic factors.

Evolving surface features resulting from oxidative growth (i.e. particle size, morphology, surface roughness, or phase composition) affect the availability and accessibility of Fe(II)-reactive sites. The comparison of particle dimensions via electron microscopy before and after reaction reveal the locations of oxidative mineral growth, which may indicate the relative Fe(II) reactivities of various facets (Chun et al. 2006; Vindedahl et al. 2015; Strehlau et al. 2016). For example, where goethite particle tips became roughened in appearance after redox, the surfaces could no longer be well-described as terminated by {021} facets that were prominent prior to reaction, rather they compose a mixture of crystal surfaces, which changes the ratio of surface sites and, therefore, affects the reaction rate (Chun et al. 2006).

Recurrent-exposure reactions are a valuable tool for evaluating the evolving reactivity of mineral surfaces. As an example, two studies investigating the evolving reactivity of goethite in 1 mM Fe(II) after five exposures of 100 μM 4-ClNB report decreasing reaction rates with each

exposure (Chun et al. 2006; Vindedahl et al. 2015). Both these studies, however, did not include pH readjustment after each sequential spike, which is expected to affect reaction kinetics as surface hydroxyl groups are more densely protonated at lower pH, therefore inhibiting the adsorption of Fe(II) and limiting the available reaction sites. A recent study of goethite reactivity under related conditions showed no significant change in rate across five to ten additions of 4-ClNB when the pH was readjusted after each sequential spike, suggesting the resulting oxidative mineral growth formed a balance between inhibitory surface roughening and increasing reactive surface area (Strehlau et al. 2016).

Results from the evolving reactivity of iron oxide surfaces enable a deeper understanding of how redox reactions at the water-mineral interface may proceed in the environment, particularly in cases where minerals have undergone substantial reactions with anthropogenic species. Here, we investigate oxidative mineral growth as a function of the availability of Fe(II)-activated surface sites at the hematite surface. The reaction variables tested include pH, Fe(II) concentration, reactive surface area, and particle morphology. Both single-exposure and recurrent-exposure reactions are performed to assess the effects of solution conditions on reactivity and to evaluate structural changes due to oxidative growth. Finally, a detailed description of the observed epitaxial growth is proposed based on lattice measurements and known geometric atomic configurations of goethite and hematite facets.

Experimental

Ultrapure water from a MilliPore Milli-Q Advantage A10 system was used for all synthesis, dialysis, and experimental processes. All solutions of HCl and NaOH for pH adjustments were

prepared from concentrated solutions of HCl (BDH Aristar, 12.1 M, 36.5 – 38.0 %) and NaOH (Fisher Scientific, 19 M, 50 % w/w). All experiments were performed in a Coy Laboratory Products vinyl anaerobic glovebag with 5 % H_2, 95 % N_2 (Matheson) atmosphere.

Hematite syntheses

Rhombohedral and equidimensional hematite particles were synthesized using procedures modified from Cornell and Schwertmann (1996). Rhombohedral particles (hereafter denoted as 'R' in tables and figures) were synthesized in a 1 L Pyrex glass bottle, where 1 L of 0.002 M HNO_3 (ACS Reagent Grade) was heated to 98 °C in an oven and 8.08 g (0.02 M Fe) of $Fe(NO_3)_3 \cdot 9H_2O$ (Sigma-Aldrich, 98 %) was added with vigorous stirring until the salt dissolved. The bottle was capped with aluminum foil (to minimize evaporation but also prevent pressurizing) then promptly returned to the 98 °C oven and heated for seven days. The foil never had contact with the solution. The suspension was cooled to room temperature, the supernatant decanted, and the concentrated suspension was dialyzed using cellulose dialysis membranes (Spectra/Por® 7, 2 kD, 38 mm × 24 mm). Dialysis water was changed nine times, with at least four hours between water changes. The suspension was transferred to a Nalgene bottle, sparged with nitrogen (Matheson 99.99 %) for two hours, and stored in the anaerobic glovebag. Equidimensional particles (hereafter denoted as 'E' in tables and figures) were synthesized in a 2 L Nalgene bottle, where 2 L of 0.002 M HCl (BDH Aristar 36.5-38.0 %) were heated to 98 °C in an oven and 10.81 g (0.02 M Fe) of $FeCl_3 \cdot 6H_2O$ (Fisher 97.3 %) was added with vigorous stirring until dissolved. Paralleling the rhombohedral synthesis, the bottle was capped with aluminum foil, promptly returned to the 98 °C oven, and heated for ten days. After cooling to

room temperature, the suspension was concentrated, dialyzed, sparged, and stored in the anaerobic glovebag.

Initial particle characterization

Following dialysis, the mass loading of each hematite stock suspension was determined as described in the Supplemental Information Section I (Fig. S1). The dried particles from the mass loading analysis were gently ground into a powder for XRD analysis. The mineral content of the powder was analyzed using a PANalytical X'Pert PRO X-ray diffractometer equipped with a cobalt source (1.7909 Å) and an X'Celerator detector. Both synthetic materials were analyzed from 10-90 ° 2θ with an effective dwell time of 100 s per step and a step size of 0.0167 ° 2θ.

Particle dimensions were determined using calibrated images collected with an FEI Tecnai T12 transmission electron microscope operating at 120 kV. TEM samples were prepared by diluting one drop of stock suspension with methanol until the suspension appeared lightly red (ca. 1000x), one drop of which was placed onto a Cu 200 mesh holey carbon grid and air-dried. Particle dimensions are reported as the average ± standard deviation of 500 measurements with approximately ten particles measured per image.

Surface area measurements were performed using N_2 adsorption by Brunauer-Emmett-Teller (BET) analysis on a Quantachrome Autosorb iQ2-MP at 77 K with outgassing at 90 °C for 12 h. Specific surface areas were determined using the adsorption branch from $P/P_o = 0.1$ to 0.28.

Batch reactor preparation

Batch reactors were prepared in 120 mL serum bottles capped with PTFE-lined rubber septa and magnetically stirred with PTFE-coated stirbars at a rate of 500 rpm. All reactors contained a buffer of 10 mM $NaHCO_3$ (Sigma-Aldrich 99.7 %) adjusted to pH 7.0 ± 0.1 with 1 M HCl. Particle surface area loading varied from 0.007 m^2/mL – 0.043 m^2/mL, which corresponds to mass loading of 0.100 to 0.600 mg/mL for rhombohedral particles and 0.383 to 1.149 mg/mL for equidimensional particles. The 175 mM Fe(II) stock solution was prepared from oxygen-free solid $FeCl_2$•$9H_2O$ (Fisher 101.5 %) and 0.3 M HCl. Reactors contained Fe(II) concentrations of 0.25, 0.50, or 1.00 mM. Reactors were loaded with hematite, pH buffer, and Fe(II), and then pH adjusted, as needed, to 7.0 or 6.5 ± 0.1 using 1 M HCl or 0.5 M NaOH.

Single-exposure and recurrent-exposure reaction sets

Reactors receiving one spike of 4-ClNB (Acros Organics 99 %) are termed single-exposure reactions and were prepared in duplicate along with an additional control reactor to which no 4-ClNB was added. All prepared reactors equilibrated for 21 hours prior to 4-ClNB addition. A 10 mM 4-ClNB stock solution prepared in methanol (Fisher Chemical 99.9 %), was added to the reactors to achieve an initial concentration of one-tenth the reactor Fe(II) concentration. Reactors receiving multiple additions of 4-ClNB were labeled recurrent-exposure reactions. For these, three to five serum bottles were identically prepared under the desired reaction conditions. One reactor functioned as a control, with no injection of 4-ClNB nor additional Fe(II). The remaining reactors received additions of 4-ClNB and sacrificed for post-reaction characterization after one, two, three, or six exposures. To perform the reaction sequence, the prepared reactors equilibrated for 21 hours, and then the appropriate amount of 4-ClNB stock solution was added

(10 % of the initial Fe(II) concentration). The first reactor in each sequence was monitored by HPLC to determine the 4-ClNB transformation rate. After 24 hours, the first reactor was tested for the presence of 4-ClNB again by HPLC. If 4-ClNB was no longer detected, the Fe(II) concentration was measured by UV-visible spectroscopy and the amount of Fe(II) needed to return the reactors to the initial Fe(II) concentration was added to all remaining reactors. Finally, the pH was adjusted to 7.0 ± 0.1 with 0.5 M NaOH. The remaining reactors equilibrated for 21 hours before the next addition of 4-ClNB, and the process was repeated. After determining the 4-ClNB reaction rate in a reactor, it was sacrificed for post-reaction characterization. The control was sacrificed along with the last reactor in the set. For a schematic describing the recurrent-exposure process, see Fig. S2.

Reaction kinetics

Reaction kinetics were monitored by quantifying 4-ClNB concentration using high-performance liquid chromatography on an Agilent 1220 Infinity equipped with Zorbax SB-C18 4.6 × 150 mm, 5-μm column. The eluent was composed of a 30 : 70 mixture of 12 mM ammonium acetate (Sigma-Aldrich 97 %) in 90 vol% water and 10 vol% acetonitrile adjusted to pH 7.0 with ammonium hydroxide (Sigma-Aldrich 28 %) : pure acetonitrile. The flow rate was 0.7 mL/min, and the detection wavelength was set to 254 nm. Standards with a concentration range of 5 – 100 μM 4-ClNB were made in methanol. For sampling, 0.5 mL of the reaction mixture was filtered into autosampler vials using PALL Life Sciences Acrodisc® 13 mm syringe filters with 0.2 μm nylon membrane starting 1 min after the 4-ClNB injection and continued until approximately 80 % of the 4-ClNB had been reduced (1 – 3 hours).

208

209 **Fe(II) adsorption**

210

211 The concentration of Fe(II) in the reactors was determined via the ferrozine assay and UV-
212 visible spectroscopy on an Agilent 8453 equipped with tungsten and deuterium lamps. A 10 mM
213 ferrozine (3-(2-pyridyl)-5,6-diphenyl-1,2,4-triazine-p,p'-disulfonic acid monosodium salt
214 hydrate, Sigma-Aldrich 97 %) was prepared in water. To remove suspended particles, 0.8 mL of
215 the reaction mixture was filtered through PALL Life Sciences Acrodisc® 13 mm syringe filters
216 with 0.2 μm nylon membrane. Polypropylene cuvettes measuring 1 cm wide were prepared in
217 triplicate with 0.4 mL of 10 mM ferrozine, 3.4 mL water, and 0.2 mL of filtered reaction
218 mixture. Standards prepared with ferrozine, water, and 0.15 mM $FeCl_2$ (diluted from 175 mM
219 stock $FeCl_2$ solution) ranged 0.005-0.050 mM Fe(II). Absorption at 562 nm was recorded in
220 triplicate for each cuvette. The Fe(II) concentration in the reaction mixture was analyzed prior to
221 4-ClNB addition and after the reaction was complete.

222

223 **Post-reaction characterization**

224

225 Particles were collected from sacrificed reactors by centrifugation using an Eppendorf 5804
226 centrifuge programmed to run at 4427 rcf for four minutes. The reactor contents were first
227 concentrated in a 50 mL centrifuge tube using up to three rounds of centrifugation, where the
228 tube was only opened under anaerobic atmosphere to decant the supernatant. Once concentrated,
229 the particles were washed four times with 35 mL aliquots of deoxygenated water, again only

decanted under anaerobic atmosphere. After the final wash, the tubes were opened to ambient atmosphere, the supernatant decanted, and the concentrated slurry transferred to weigh boats to dry at room temperature in a fume hood. A portion of the dried particles was gently ground to produce a uniform powder for XRD analysis. For TEM analysis, a minute quantity of unabraded powder was added to 0.5 mL of methanol and sonicated for 30 seconds or until the suspension appeared light red. For electron diffraction, the same suspension was sonicated for 15 minutes to assist in separating the rods from the larger particles. To prepare the samples for TEM analysis, one drop of the suspension was placed onto a Cu 200 mesh holey carbon grid, allowed to dry overnight, and analyzed on an FEI Technai T12 transmission electron microscope operated at 120 kV.

XRD calibration curve

An X-ray diffraction calibration curve was used to quantify hematite and goethite present after reaction. Calibration standards containing 1 – 50 mass% goethite were prepared from aqueous suspensions using mixtures of goethite (10.00 mg/mL) and rhombohedral hematite (3.93 mg/mL). Goethite (space group Pnma) was obtained from the starting material used for experiments described in Penn et al. (2006), and the particles had average dimensions of 90 nm by 10 nm. Two standards were prepared with equidimensional hematite (8.29 mg/mL) to test comparability. All standards and reaction samples were analyzed from 18-32° 2θ with an effective dwell time of 950 s per step and a step size of 0.0167° 2θ. The (110) reflection of goethite (at 24° 2θ with the Co source) and (012) reflection of hematite (at 28° 2θ with the Co source) were chosen because of the strong scattering intensity and baseline separation from other

goethite and hematite reflections. Origin (OriginLab Corporation 2016, version 93E) was used to zero the spectral background, and the peaks were individually fitted using the PsdVoigt1 function to obtain integrated peak areas. Peak areas were multiplied by the goethite (110) and hematite (012) structure factors squared to correct for relative peak intensities, which were calculated to be 31.9 and 102.9, respectively. See Supplemental Section II for a detailed description of these calculations.

Results

Initial hematite particle characterization

Hematite particles with two different morphologies were successfully synthesized. Collected XRD patterns for the as-synthesized materials are both consistent with the hematite PDF 33-0664 (Fig. S3). No additional phases were detected. The rhombohedral hematite particle dimensions were 43 ± 8 nm by 29 ± 6 nm, and the nominally equidimensional hematite particles had a diameter measuring 88 ± 13 nm. See Fig. S4 for graphics describing measurement geometry and particle size distribution. Specific surface areas were determined using N_2 adsorption and were 72.3 m^2/g and 18.9 m^2/g for rhombohedral and equidimensional hematite, respectively.

Based on TEM images and electron diffraction patterns, the rhombohedral hematite particles are well described as rhombohedra with a slightly truncated pseudocubic morphology, which is a hybrid of two morphologies described by Guo and Barnard (2011). Purely rhombohedral hematite is bound only by {101} facets, while fully truncated pseudocubic morphologies have

sizeable {012} facets at the far tips of the rhombohedra. TEM images of the particles used here (Fig. S5) show only minor {012} facets, giving the particles a mostly rhombohedral morphology. The crystallographic structure of hematite dictates that the {101} and {012} planes are orthogonal, which is consistent with the lattice fringe spacings observed in TEM images (Fig. S5) as well as the observation that the {012} lattice fringes are perpendicular to the adjacent {101} facets of the rhombohedron. For the equidimensional particles, tilt series confirm the equidimensional morphology, rather than a plate-like structure (not shown).

Oxidative mineral growth on hematite nanoparticles

The products of the oxidative mineral growth are a mixture of goethite and hematite, and the relative amount of each mineral was tracked as a function of Fe(II) concentration, surface area loading, pH, and the morphology (rhombohedral vs equidimensional) of the hematite particle. The reference condition, which was selected because it is consistent with the aqueous conditions used in previous work with goethite (Vindedahl et al. 2015; Strehlau et al. 2016), used the rhombohedral particles with surface area loading of 0.0072 m^2/mL (0.100 mg/mL mass loading) and 1 mM Fe(II) at pH 7.0 with one exposure of 100 μM 4-ClNB, and is hereafter denoted R-r. The post-reaction solid contained 15(2) % goethite by mass as determined by XRD.

Growth as a function of reaction conditions.

To quantitively compare the products of oxidative growth as a function of reaction conditions, the stoichiometric maximum of goethite that could be produced by oxidative mineral growth, expressed as a mass percent in the final solid after the reaction has gone to completion, was calculated. For each reaction condition, the stoichiometric mass percent of goethite was

299 calculated using the following restrictions: (1) all six electrons needed for the reduction of 4-
300 ClNB are provided through Fe(II) oxidizing to Fe(III) and (2) all Fe(III) is incorporated into the
301 crystal structure as α-FeOOH. For example, the stoichiometric maximum for R-r is 35 mass%
302 goethite after the reaction has gone to completion. The stoichiometric maximum of goethite for
303 each reaction condition is reported in Table 1 as goethite max (mass%). The difference in
304 aqueous Fe(II) measured before and after reaction is stoichiometrically consistent with the Fe(II)
305 mass balance (Fig. S6).

306 Set a (Table 1) tested the effect of increased surface area loading for a single-exposure
307 reaction of 100 μM 4-ClNB with 1 mM Fe(II) at pH 7.0. When the surface area loading was
308 doubled (R-a1) as compared to the reference condition, the formation of goethite decreased
309 substantially, with only trace goethite (< 1 mass%) detected by XRD. In reactors prepared with
310 even higher surface area loading (i.e. R-a2, R-a3, and R-a4), no goethite was detected. TEM
311 micrographs of the post-reaction material support this result, with few rods observed in R-a1 and
312 no rods observed in post-reaction material from R-a2, R-a3, and R-a4 (Fig. S7). With high
313 surface area loading, it is possible that Fe(III) is incorporated as goethite layers too thin to be
314 detected either in TEM images or through XRD. Indeed, a quick calculation assuming 37 nm
315 spherical particles yields approximately a 1 nm shell distributed over the entire particle surface.
316 As such, recurrent-exposure reactions were used to further probe high surface area loading
317 conditions, where the ratio of total oxidized Fe(II) to initial hematite mass is held constant.

318 Set b (Table 1) tested the effect of increased surface area loading in recurrent-exposure
319 reactions, with the cumulative stoichiometric maximum of goethite equal to R-r, at 35 mass%.
320 Sequence R-b1 contained three times the surface area loading as R-r and received three additions
321 of 100 μM 4-ClNB, and sequence R-b2 contained six times the surface area loading as R-r and

received six additions of 4-ClNB. In comparison to R-r, there was a decrease in the observed goethite content: from 15(2) mass% for one exposure in R-r, to 9.3(8) mass% for three exposures in R-b1, and 1.9(4) mass% for six exposures in R-b2 (Fig. 1).

Set c (Table 1) tested the effect of decreased pH by using an initial pH of 6.5 while matching all other variables of the reference reaction. After reaction, only trace goethite was detected (< 1 mass%) by XRD. TEM micrographs of the R-c1 post-reaction material supports this result, with few rods observed (Fig. S7).

Set d (Table 1) tested the effect of decreased aqueous Fe(II) concentration. Two recurrent-exposure experiments were prepared; as compared to the reference, the Fe(II) and 4-ClNB concentrations were halved and two exposures were performed in R-d1, and the concentrations were quartered with four exposures performed in R-d2. For both sequences, the stoichiometric maximum of goethite was 35 mass%. All reactors in R-d1 and R-d2 were analyzed by XRD for mineral content, and the trends are presented in Fig. 2. At halved concentrations, only trace goethite (<1 mass%) was observed after the first exposure while the vast majority of the observed goethite formed during the second exposure, giving a total observed goethite in R-d1 of 9(1) mass%. At quartered concentrations, there was no detectable goethite formed after either the first or second exposure, but 2.3(5) mass% was observed after the third exposure, and the remaining goethite formed in the fourth exposure to total 6.2(8) mass% in R-d2. The data presented in Fig. 2 show two main points: (1) as Fe(II) concentration decreases, less goethite is formed, and (2) under recurrent-exposure conditions, goethite forms later in the exposure sequence.

Set e (Table 1) tested how the aforementioned surface area loading results compare with hematite of a different morphology, given that the exposed surfaces are quite different. The

single-exposure condition (E-e1) and recurrent-exposure condition (E-e2) were matched in surface area loading to the rhombohedral reference R-r (0.0072 m^2/mL) and recurrent-exposure R-b1 (0.0217 m^2/mL) as calculated from the BET measurements. Due to the larger particle size of equidimensional hematite, and thus higher mass loading, the stoichiometric maximum of goethite for each condition was 12 mass%. Condition E-e1 produced 5.2(7) mass% goethite and condition E-e2 produced 1.9(4) mass% goethite.

Comparing reactors that have equivalent ratio of oxidized Fe(II) to surface area loading demonstrates that the goethite mass percent formed on rhombohedral and equidimensional hematite are both negatively correlated with an increase in surface area loading (Fig. 3). The stoichiometric maxima of goethite for all reactors in Set b and Set e are 35 mass% and 12 mass%, respectively. The observed mass percent of goethite in each sample was lower than the stoichiometric maximum, and some samples showed a trend: in the single-exposure experiments with rhombohedral and equidimensional hematite (0.0072 m^2/mL surface area loading), approximately 45 % of the stoichiometric maximum goethite formation was observed. In recurrent-exposure experiments (0.0217 m^2/mL surface area loading), approximately 27 % of the stoichiometric maximum goethite formed on the rhombohedral particles and 16 % formed on the equidimensional particles.

Supporting the trends in oxidative mineral growth observed by XRD, TEM micrographs show that the length and number of rod-like particles in the post-reaction material for both Set b and Set e decreases as the surface area loading increases (Fig. 3). Images of samples containing pure hematite (R, E of Fig. 3) exhibited no particles with the rod morphology characteristic of goethite. There was no detectable goethite by XRD or TEM in any of the control reactors.

Reaction kinetics

The effects of solution conditions on hematite reactivity were studied in both single-exposure and recurrent-exposure experiments. For comparison, literature values for goethite reactivity (Table S1) were selected with the restrictions that mineral size and solution conditions were similar to the conditions used in this study (Chun et al. 2006; Stemig et al. 2014; Vindedahl et al. 2015). All rates are normalized to reactor surface area loading (m^2/mL).

Single-exposure reaction kinetics.

The single-exposure reduction rate of 4-ClNB by Fe(II) in suspensions containing rhombohedral and equidimensional hematite increases as the surface area loading increases, as seen in Fig. 4a, which correlates with an increase in the number of available reactive sites. When compared to reactions using goethite and 4-ClNB, rhombohedral and equidimensional hematite react faster than goethite (Fig. 4a).

Recurrent-exposure reaction kinetics.

In the recurrent-exposure experiments of 4-ClNB on both rhombohedral and equidimensional hematite (Fig. 4b), reaction rates drop substantially over the course of the exposure sequence. For the first exposure, Fig. 4b shows again that as surface area loading increases, reaction rate increases. For further 4-ClNB exposures, reaction rates progressively decrease with each exposure. In the recurrent-exposure experiment containing R-b2, reactors were sacrificed for determining the 4-ClNB reduction rate after one, three, and six exposures. The rate dropped from 2.7(4) h^{-1} for the first exposure to 1.6(2) h^{-1} and 1.5(2) h^{-1} in the third and sixth exposure,

respectively. Further, in the recurrent-exposure experiment containing R-b1, the reaction rate decreased from 2.0(3) h^{-1} in the first exposure to 1.2(2) h^{-1} after the third exposure. In both R-b1 and R-b2, the observed rates decrease to approximately 60 % of the initial rate. In the recurrent-exposure experiment with equidimensional hematite, the rate decreased from 2.0(3) h^{-1} in the first exposure to 0.7(1) h^{-1} then 0.9(1) h^{-1} after the second and third exposures, respectively. These rates were both approximately 40-50 % of the initial rate.

Post-reaction mineral identification by TEM

TEM imaging shows that many of the rhombohedral particles have a 'kite-and-tail' morphology after reaction with 4-ClNB, as seen in Fig. 5a. The tails, composed of newly-formed material on hematite {012}, are referred to as rods within this work. Selected area diffraction of extensively sonicated samples enabled facile collection of diffraction patterns of the rods (Fig. 5b, left inset), which were consistent with the goethite crystal structure in all tested samples (more examples given in Fig. S8). Lattice fringe measurements indicated the presence of goethite in both rhombohedral and equidimensional post-reaction specimens, with the (110) (Fig. 5b, right inset) and the (040) lattice planes (Fig. S8) aligned with the growth direction, which is consistent with the known elongation direction of goethite.

Discussion

Contrary to what has been previously reported (Larese-Casanova et al. 2012), the mass fraction of goethite in the post-reaction solids depended strongly on the reaction conditions: the

observed goethite mass percent in the post-reaction material decreased when surface area loading increased, when initial pH decreased, and when the aqueous Fe(II) concentration decreased. The difference between these results may be attributed to the conditions employed, which differed in buffer identity (3-(*N*-morpholino)propanesulfonic acid), mass loading (>3×), Fe(II) concentration (3×), and pH (>7.0). These results indicate that the heterogeneous nucleation of new phases on the hematite surface is dependent on the distribution of Fe(II)-activated surface sites in aqueous suspensions containing carbonate.

Fe(II)-activated surface site geometry

Structural considerations support the notion that the atomic surface geometry of hematite {012} serves as an epitaxial template for goethite formation. The specific adsorption of Fe(II) is known to occur at the contiguous singly-coordinated hydroxyl group pair sites (Wehrli et al. 1989; Barron and Torrent 1996); both goethite {021} and hematite {012} have approximately four contiguous singly-coordinated hydroxyl group pairs per nm^2 (Table 2). The Fe atoms directly below these contiguous singly-coordinated hydroxyl groups are positioned at equivalent distances below the outermost oxygen atoms, at 0.178 and 0.177 nm in hematite and goethite, respectively (Fig. 6). Additionally, these contiguous singly-coordinated hydroxyl group pairs have the same spatial positioning above their coordinated Fe(III). Hematite {012} has equivalent surface densities of triply- and singly-coordinated hydroxyl groups, at 7.3 hydroxyl groups per nm^2, and no doubly-coordinated groups (Barron and Torrent 1996). The addition of new Fe(III) at only one-half the hydroxyl groups on hematite {012} produces a layer of material that has structural similarity to goethite, which has approximately one-half the Fe density of hematite. Indeed, equilibrium experiments have shown a plateau in the maximum adsorption of

Fe(II) on hematite {012} where roughly half of the available binding sites were occupied (Tanwar et al. 2008). These structural similarities are crystallographically consistent with the observed transition in phase composition from hematite to goethite.

Rhombohedral hematite is one of the least thermodynamically favored hematite morphologies (Guo and Barnard 2011). Because of the high free energy of formation and high surface energies relative to goethite (Navrotsky et al. 2008; Guo and Barnard 2011), substantial growth of the existing hematite crystal is unlikely in aqueous conditions at room temperature. Additionally, goethite formation is favorable in aqueous systems containing carbonate (Cornell and Schwertmann 1996). There are, however, substantial gaps in understanding this phase transformation. Detailed thermodynamic calculations and modeling are needed, because reactive surface structures are a function of Fe(II) concentration, equilibration time, peripheral ion concentrations, pH, and extent of reaction with oxidized molecules, and the nature of evolving reactivity calls for an iterative approach to such calculations.

Reaction kinetics

Faster reaction rates observed with higher surface area loading is expected because a greater number of reaction sites allows more Fe(II) adsorption to occur and, thus, more electron transfer to the bulk and more rapid 4-ClNB reduction. Differences in 4-ClNB reduction rates between these results with hematite and literature rates for goethite (normalized for surface area loading) arises from the differences in reactivity across accessible facets. For goethite, the majority of oxidative mineral growth occurs on {021} rather than {110} in circumneutral pH conditions in the absence of species that inhibit Fe(II) adsorption and/or the approach of the contaminant (e.g. dissolved organic matter; Strehlau et al. 2016). The {021} of the goethite crystals comprise a

minor fraction of the accessible surface area. The faster rate observed for the reaction on rhombohedral hematite could mean that either a greater fraction of the total accessible surface area adsorbs Fe(II) or the secondary facets adsorb more Fe(II) than those on goethite, or both.

In recurrent-exposure experiments with hematite, the dramatic decrease in reaction rate between the first and third exposures of 4-ClNB is a consequence of the changing distribution and identity of accessible reactive sites. Initially, the surface is solely comprised of hematite. Once goethite sites form, the reaction rate slows as hematite surface sites are blocked by the goethite, and the more slowly reacting goethite surface sites comprise an increasing fraction of the total accessible surface sites. This is shown in Fig. 4, where recurrent-exposure reaction rates (Fig. 4b) decrease to a level fitting the trend of goethite rates (Fig. 4a). Growth formed through further reactions would not be expected to have a substantial impact on rate, even as the goethite surface area increases slightly. Indeed, previous studies have shown that goethite rate remains relatively constant over pH-controlled recurrent-exposure reactions (Strehlau et al. 2016).

Implications

The evolving reactivity of hematite and goethite nanoparticles in anoxic aqueous environments is important for applications in pollutant fate modeling. Projecting the fate and transport of oxidized contaminants and their products in groundwater systems containing iron oxides requires a detailed understanding not only of the chemical transformation of the contaminant but also the characteristics of reactive sites on mineral surfaces and how those characteristics change as reactions progress.

Specifically addressing the water-mineral interface, the reactivity of iron oxide surfaces is sensitive to aqueous conditions such as Fe(II) concentration, pH, and availability of accessible surface sites. The reactivity of the minerals, however, is determined by what surfaces are present at a particular time. As the exposed surfaces grow or dissolve, the reactivity of the system evolves and disordered or roughened surfaces lead to substantial changes in the kinetics of contaminant reduction and concurrent oxidative mineral growth. Under conditions that favor hematite production on hematite nanoparticles, reactivity is expected to be relatively unchanging. Conditions that favor goethite production on hematite surfaces, however, could lead to vastly different reaction rates; a hematite particle coated in a goethite shell would behave as goethite, regardless of which mineral is present in larger mass.

With two mineral phases present, the most important parameter is accessible surface area of the respective minerals. As reactions progress, however, this parameter is a moving target. Ultimately, the aqueous conditions determine which mineral phase forms on the hematite particles, and those conditions can be used to predict reactivity based on evolving mineralogy. Illustrated by the results presented here for hematite particles, fate models for contaminated ground water systems should consider not only initial mineral composition and surface area at the time of contaminant exposure but also the minerals that may form as a result of surface reactions to predict changes in pollutant transformation rates.

Acknowledgements

This work was funded by the NSF grant ECS-1012193 and CHE-1507496. Parts of this work were carried out in the Characterization Facility, University of Minnesota, which receives

505 partial support from NSF through the MRSEC program. Thanks to Thomas E. Webber, who
506 performed the BET measurements.

507

508 **References**

509

510 Barron, V., and Torrent, J. (1996) Surface Hydroxyl Configuration of Various Crystal Faces of
511 Hematite and Goethite. Journal of Colloid and Interface Science, 177, 407–410.
512 Boparai, H.K., Comfort, S.D., Shea, P.J., and Szecsody, J.E. (2008) Remediating explosive-
513 contaminated groundwater by in situ redox manipulation (ISRM) of aquifer sediments.
514 Chemosphere, 71, 933–941.
515 Catalano, J.G., Fenter, P., Park, C., Zhang, Z., and Rosso, K.M. (2010) Structure and oxidation
516 state of hematite surfaces reacted with aqueous Fe(II) at acidic and neutral pH. Geochimica
517 et Cosmochimica Acta, 74, 1498–1512.
518 Chopard, A., Benzaazoua, M., Bouzahzah, H., Plante, B., and Marion, P. (2017) A contribution
519 to improve the calculation of the acid generating potential of mining wastes. Chemosphere,
520 175, 97–107.
521 Chun, C.L., Penn, R.L., and Arnold, W.A. (2006) Kinetic and Microscopic Studies of Reductive
522 Transformations of Organic Contaminants on Goethite. Environmental Science and
523 Technology, 40, 3299–3304.
524 Cornell, R.M., and Schwertmann, U. (1996) The Iron Oxides, 360 p. Wiley-VCH, Weinheim,
525 Germany.
526 Dunnivant, F.M., Schwarzenbach, R.P., and Macalady, D.L. (1992) Reduction of Substituted
527 Nitrobenzenes in Aqueous Solutions Containing Natural Organic Matter. Environmental

528 Science and Technology, 26, 2133–2141.
529 Elsner, M., Haderlein, S.B., Kellerhals, T., Luzi, S., Zwank, L., Angst, W., and Schwarzenbach,
530 R.P. (2004a) Mechanisms and Products of Surface-Mediated Reductive Dehalogenation of
531 Carbon Tetrachloride by Fe(II) on Goethite. Environmental Science and Technology, 38,
532 2058–2066.
533 Elsner, M., Schwarzenbach, R.P., and Haderlein, S.B. (2004b) Reactivity of Fe(II)-bearing
534 minerals toward reductive transformation of organic contaminants. Environmental Science
535 and Technology, 38, 799–807.
536 Faivre, D. (2016) Introduction. In D. Faivre, Ed., Iron Oxides: From Nature to Applications, p. 1-
537 5. Wiley - VCH, Weinheim, Germany.
538 Guo, H., and Barnard, A.S. (2011) Thermodynamic modelling of nanomorphologies of hematite
539 and goethite. Journal of Materials Chemistry, 21, 11566.
540 Hofstetter, T.B., Heijman, C.G., Haderlein, S.B., Holliger, C., and Schwarzenbach, R.P. (1999)
541 Complete reduction of TNT and other (poly)nitroaromatic compounds under iron-reducing
542 subsurface conditions. Environmental Science and Technology, 33, 1479–1487.
543 Howard, P.H., and Muir, D.C.G. (2013) Identifying New Persistent and Bioaccumulative
544 Organics Among Chemicals in Commerce. III: Byproducts, Impurities, and Transformation
545 Products. Environmental Science and Technology, 47, 5259–5266.
546 Jeon, B.H., Dempsey, B.A., Burgos, W.D., and Royer, R.A. (2001) Reactions of Ferrous Iron
547 with Hematite. Colloids and Surfaces A: Physicochemical and Engineering Aspects, 191,
548 41–55.
549 Jeon, B.H., Dempsey, B.A., and Burgos, W.D. (2003) Kinetics and mechanisms for reactions of
550 Fe(II) with iron(III) oxides. Environmental Science and Technology, 37, 3309–3315.

551 Ju, K.-S., and Parales, R.E. (2010) Nitroaromatic compounds, from synthesis to biodegradation.
552 Microbiology and Molecular Biology Reviews, 74, 250–72.
553 Klausen, J., Troeber, S.P., Haderlein, S.B., and Schwarzenback, R.P. (1995) Reduction of
554 Substituted Nitrobenzenes by Fe(II) in Aqueous Mineral Suspensions. Environmental
555 Science and Technology, 29, 2396–2404.
556 Lagroix, F., Banerjee, S.K., and Jackson, M.J. (2016) Geological Occurrences and Relevance of
557 Iron Oxides. In Iron Oxides: From Nature to Applications p. 7–30., Wiley - VCH,
558 Weinheim, Germany.
559 Larese-Casanova, P., and Scherer, M.M. (2007) Fe(II) sorption on hematite: New insights based
560 on spectroscopic measurements. Environmental Science and Technology, 41, 471–477.
561 Larese-Casanova, P., Kappler, A., and Haderlein, S.B. (2012) Heterogeneous oxidation of Fe(II)
562 on iron oxides in aqueous systems: Identification and controls of Fe(III) product formation.
563 Geochimica et Cosmochimica Acta, 91, 171–186.
564 Maqueda, C., Undabeytia, T., Villaverde, J., and Morillo, E. (2017) Behaviour of glyphosate in a
565 reservoir and the surrounding agricultural soils. Science of the Total Environment, 593–594,
566 787–795.
567 Navrotsky, A., Mazeina, L., and Majzlan, J. (2008) Size-Driven Structural and Thermodynamic
568 Complexity in Iron Oxides. Science, 319, 1635–1638.
569 Pauling, L., and Hendricks, S.B. (1925) The Crystal Structures of Hematite and Corundum.
570 Journal of the American Ceramic Society, 47, 781-790.
571 Pecher, K., Haderlein, S.B., and Schwarzenbach, R.P. (2002) Reduction of polyhalogenated
572 methanes by surface-bound Fe(II) in aqueous suspensions of iron oxides. Environmental
573 Science and Technology, 36, 1734–1741.

574 Pedersen, H.D., Postma, D., Jakobsen, R., and Larsen, O. (2005) Fast transformation of iron
575 oxyhydroxides by the catalytic action of aqueous Fe(II). Geochimica et Cosmochimica
576 Acta, 69, 3967–3977.
577 Penn, R.L., Erbs, J.J., and Gulliver, D.M. (2006) Controlled Growth of alpha-FeOOH Nanorods
578 by Exploiting-Oriented Aggregation. Journal of Crystal Growth, 293, 1–4.
579 Rosso, K.M., Smith, D.M.A., and Dupuis, M. (2003) An ab initio model of electron transport in
580 hematite (α-Fe2O3) basal planes. Journal of Chemical Physics, 118, 6455–6466.
581 Rosso, K.M., Yanina, S. V., Gorski, C.A., Larese-Casanova, P., and Scherer, M.M. (2010)
582 Connecting observations of hematite (α-Fe2O3) growth catalyzed by Fe(II). Environmental
583 Science and Technology, 44, 61–67.
584 Scherer, M.M., Richter, S., Valentine, R.L., and Alvarez, P.J.J. (2000) Chemistry and
585 Microbiology of Permeable Reactive Barriers for In Situ Groundwater Clean up. Critical
586 Reviews in Environmental Science and Technology, 30, 363–411.
587 Schwertmann, U., and Murad, E. (1983) Effect of pH on the Formation of Goethite and Hematite
588 from Ferrihydrite. Clays and Clay Minerals, 31, 277–284.
589 Stemig, A.M., Do, T.A., Yuwono, V.M., Arnold, W.A., and Penn, R.L. (2014) Goethite
590 Nanoparticle Aggregation: Effects of Buffers, Metal Ions, and 4-Chloronitrobenzene
591 Reduction. Environmental Science: Nano, 1, 478–487.
592 Strehlau, J.H., Stemig, M.S., Penn, R.L., and Arnold, W.A. (2016) Facet-Dependent Oxidative
593 Goethite Growth As a Function of Aqueous Solution Conditions. Environmental Science
594 and Technology, 50, 10406–10412.
595 Strehlau, J.H., Schultz, J.D., Vindedahl, A.M., Arnold, W.A., and Penn, R.L. (2017) Effect of
596 nonreactive kaolinite on 4-chloronitrobenzene reduction by Fe(II) in goethite–kaolinite

heterogeneous suspensions. Environmental Science: Nano, 4, 325–334.

Szytula, A., Bureqicz, A., Dimitrijevic, Z., Krasnicki, S., Rzany, H., Todorovic, J., Wanic, A., and Wolski, W. (1968) Neutron Diffraction Studies of α-FeOOH. Physica Status Solidi, 26, 429-434.

Tanwar, K.S., Petitto, S.C., Ghose, S.K., Eng, P.J., and Trainor, T.P. (2008) Structural study of Fe(II) adsorption on hematite(1-102). Geochimica et Cosmochimica Acta, 72, 3311–3325.

Valencia-Avellan, M., Slack, R., Stockdale, A., and Mortimer, R.J.G. (2017) Understanding the mobilisation of metal pollution associated with historical mining in a carboniferous upland catchment. Environmental Science: Processes Impacts, 19, 1061–1074.

Vindedahl, A.M., Arnold, W.A., and Penn, R.L. (2015) Impact of pahokee peat humic acid and buffer identity on goethite aggregation and reactivity. Environmental Science: Nano, 2, 509–517.

Wehrli, B., Sulzberger, B., and Stumm, W. (1989) Redox processes catalyzed by hydrous oxide surfaces. Chemical Geology, 78, 167–179.

West, A.R. (2014) Solid State Chemistry and its Applications, p. 248-258. Wiley, U.K.

Williams, A.G.B., and Scherer, M.M. (2004) Spectroscopic Evidence for Fe(II)-Fe(III) Electron Fransfer at the Iron Oxide-Water Interface. Environmental Science and Technology, 38, 4782–4790.

Yang, H., Lu, R., Downs, R.T., and Costin, G. (2006) Goethite, α-FeO(OH), from single-crystal data. Acta Crystallographica Section E: Structure Reports Online, 62.

This is a preprint, the final version is subject to change, of the American Mineralogist (MSA)
Cite as Authors (Year) Title. American Mineralogist, in press.
DOI: https://doi.org/10.2138/am-2018-6342

620

621
622
623
624
625
626

627 **Table 1.** Summary of reaction conditions in suspensions of rhombohedral (R) and
628 equidimensional (E) hematite, with final goethite mass percent in post-reaction material
629 determined using the XRD calibration curve (Fig. S11). Abbreviations are surface area loading
630 (S.A. Loading), stoichiometric maximum of goethite (Gth Max.), observed goethite (Gth Obs.),
631 and standard deviation of the observed goethite mass% across replicate reactors and/or replicate
632 XRD scans (St Dev). Dash symbol (-) indicates not detected.

633

Set	ID	Mass Loading (mg/mL)	S.A. Loading (m^2/mL)	# Exposures, ([4-ClNB] μM)	pH	Fe(II) (mM)	Gth Max (mass%)	Gth Obs (mass%)	St. Dev. (mass%)
Ref.	R-r	0.100	0.0072	1, (100)	7.0	1.00	35	15.4	2.2
a	R-a1	0.200	0.0145	1, (100)	7.0	1.00	21	trace	
	R-a2	0.275	0.0199	1, (100)	7.0	1.00	16	-	
	R-a3	0.300	0.0217	1, (100)	7.0	1.00	15	-	
	R-a4	0.325	0.0235	1, (100)	7.0	1.00	14	-	
b	R-b1	0.300	0.0217	3, (100)	7.0	1.00	35	9.3	0.8
	R-b2	0.600	0.0434	6, (100)	7.0	1.00	35	1.9	0.6
c	R-c1	0.100	0.0072	1, (100)	6.5	1.00	35	trace	
d	R-d1	0.100	0.0072	2, (50)	7.0	0.50	35	9.5	1.2
	R-d2	0.100	0.0072	4, (25)	7.0	0.25	35	6.2	0.8
e	E-e1	0.383	0.0072	1, (100)	7.0	1.00	12	5.2	0.7
	E-e2	1.149	0.0217	3, (100)	7.0	1.00	12	1.9	0.4

634

635 **Table 2.** Areal density of contiguous singly-coordinated hydroxyl group pairs across four Miller
636 indices of hematite and goethite with corresponding lattice spacing (Barron and Torrent 1996).

637

This is a preprint, the final version is subject to change, of the American Mineralogist (MSA)
Cite as Authors (Year) Title. American Mineralogist, in press.
DOI: https://doi.org/10.2138/am-2018-6342

Miller Index	d-Spacing (Å)	Areal Density of Contiguous Singly-Coordinated Hydroxyl Groups (pairs per nm^2)
Hem {113}	2.21	2.1
Hem {110}	2.52	2.5
Hem {100}	4.36	2.9
Hem {012}	3.68	3.7
Gth {110}	4.18	1.5
Gth {100}	4.61	1.7
Gth {010}	9.96	3.6
Gth {021}	2.58	4.1

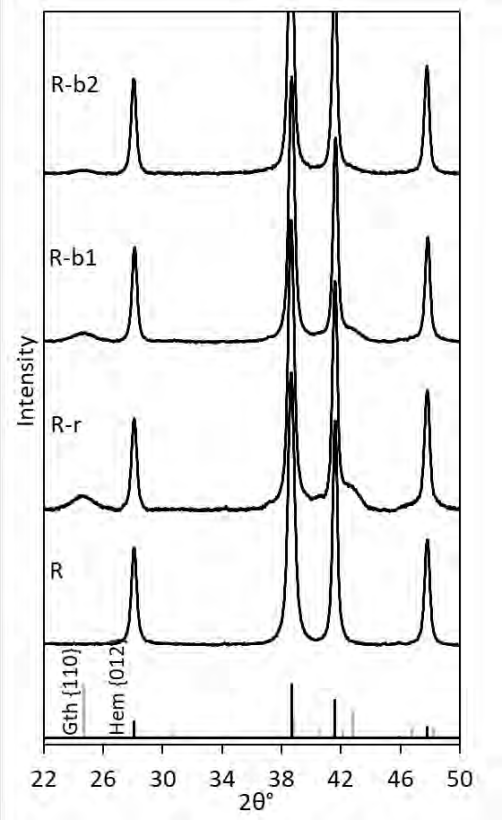

Figure 1. X-ray diffraction patterns for a recurrent-exposure set using rhombohedral hematite. Refer to Table 1 for sample identifiers. The diffraction pattern of the pure rhombohedral stock suspension is denoted R. Origin (OriginLab Corporation 2016, version 93E) was used to

644 subtract the baseline, smooth the data using 3 average-adjacent data points, and normalize each
645 pattern to the hematite {012} peak intensity. See Fig. S9 for the raw pattern of sample R-r.
646
647
648

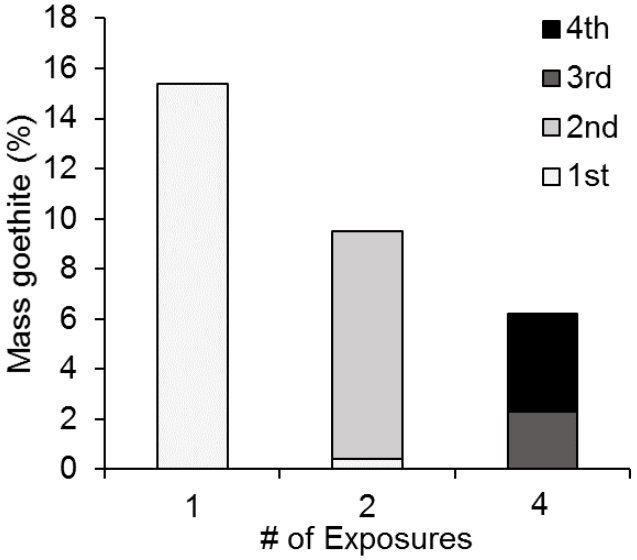

649

650 **Figure 2.** Mass% of goethite present after each exposure of 4-ClNB in the single-exposure
651 reference and in the recurrent-exposure reactors of Set d, where the Fe(II) and 4-ClNB
652 concentrations were halved and quartered as compared to the reference condition and given two
653 and four exposures, respectively.
654

This is a preprint, the final version is subject to change, of the American Mineralogist (MSA)
Cite as Authors (Year) Title. American Mineralogist, in press.
DOI: https://doi.org/10.2138/am-2018-6342

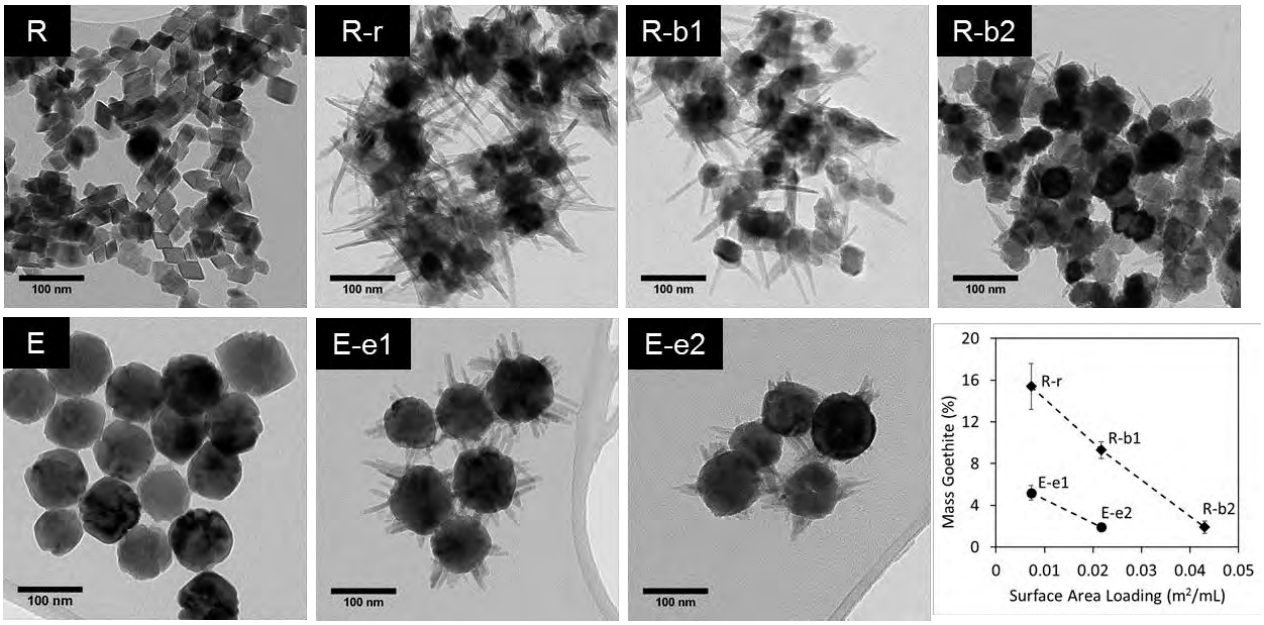

Figure 3. TEM images of solid materials collected from batch reactors prepared with the synthetic rhombohedral (R) and equidimensional (E) hematite particles. See Table 1 for corresponding sample identifiers, reactor conditions, and mineral phase quantification. The plot shows observed goethite mass percent vs reactor surface area loading for each post-reaction material shown in the given TEM images. Dashed lines are used to guide the eye for each reaction set. Error bars represent the standard deviation of replicate reactors and/or XRD scans.

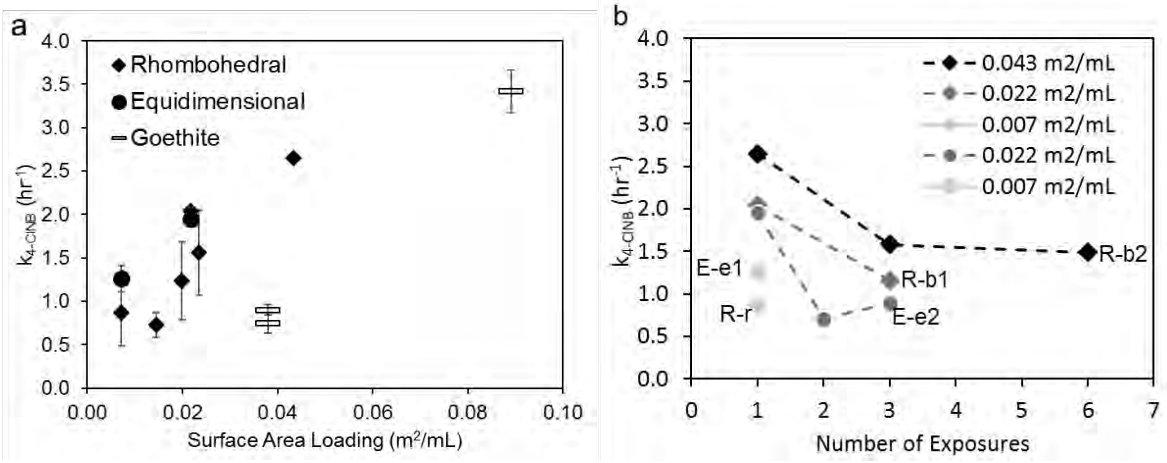

Figure 4. Reaction rate data for (a) single- and (b) recurrent-exposures of 4-ClNB on hematite nanoparticles of rhombohedral and equidimensional morphologies. Error bars represent the 95

666 % confidence interval. Dashed lines in (b) are intended to guide the eye among exposure
667 sequences. Goethite rate data points are literature values with their reported 95 % confidence
668 intervals (Chun et al. 2006; Stemig et al. 2014; Vindedahl et al. 2015).

669

670

671

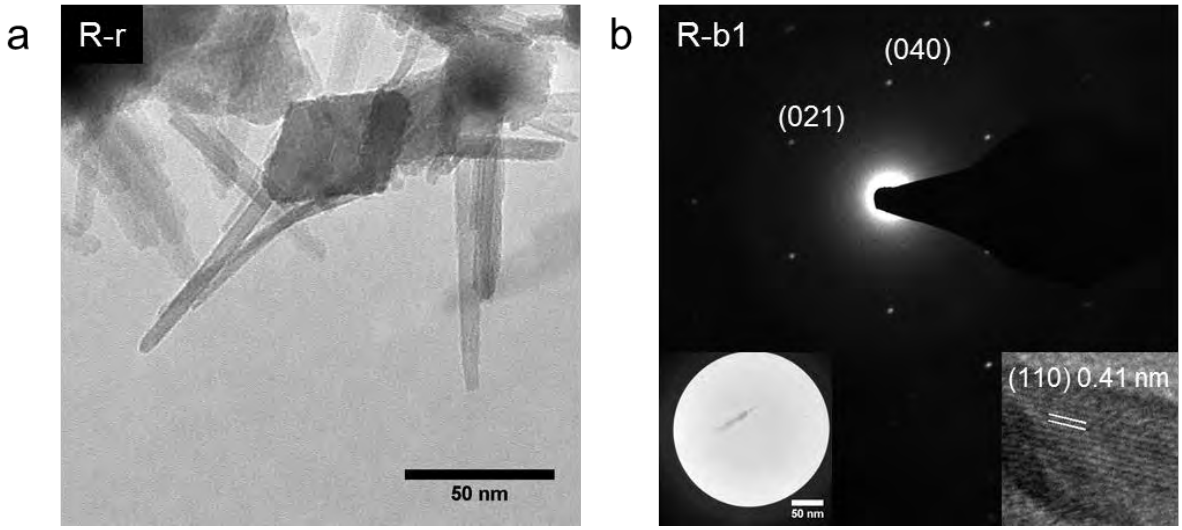

672
673 **Figure 5.** TEM images showing (a) the kite-shaped particle morphology post-reaction and (b)
674 electron diffraction pattern and crystal lattice measurements (right inset), which indicate the
675 presence of goethite. The left inset shows a selected rod aggregate that produced the diffraction
676 pattern viewed down the [100] zone axis. Additional electron diffraction patterns and crystal
677 lattice measurements for other reactors are shown in Fig. S8.

678

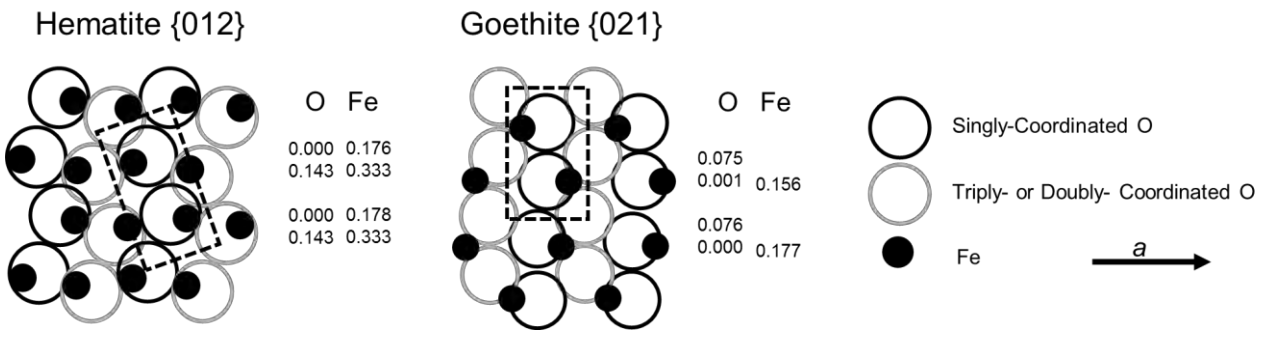

679

Figure 6. Schematic of the hematite {012} and goethite {021} surface Fe and O positions. Gray open circles indicate singly-coordinated hydroxyl groups. Black open circles indicate triply-coordinated hydroxyl groups on hematite and doubly-coordinated hydroxyl groups on goethite. Dotted-line boxes contain a pair of contiguous singly-coordinated hydroxyl groups. Columns of numbers to the right of each schematic are the distances (in nm) of the respective atoms (O or Fe) below the surface as defined by the positions of the oxygen anions labeled with 0.000. Both surfaces are positioned according to the *a* unit cell axis. Adapted from Barron and Torrent, 1996.